

High-frequency complex permeability calculation for metallic soft magnetic particles with easy magnetization plane in non-magnetic medium

Liangrui Tan(谭梁睿), Donglin He(何东霖), Zhibiao Xu(徐志彪), Guowu Wang(王国武), Shengyu Yang(杨晟宇), Shaoyong Leng(冷绍勇), Ruilong Li(李睿龙), and Tao Wang(王涛)

Citation: Chin. Phys. B, 2025, 34 (**11**): 117501. DOI: 10.1088/1674-1056/ae00ad
http://cpb.iphy.ac.cn; http://iopscience.iop.org/cpb

What follows is a list of articles you may be interested in

MHz cut-off frequency and permeability mechanism of iron-based soft magnetic composites

Xiao-Wei Jin(金校伟), Tong Li(李通), Hui-Gang Shi(史慧刚), and De-Sheng Xue(薛德胜)
Chin. Phys. B, 2024, 33 (**9**): 097501. DOI: 10.1088/1674-1056/ad57aa

Tuning magneto-dielectric properties of Co_2Z ferrites via Gd doping for high-frequency applications

Jian Wu(武剑), Bing Lu(卢冰), Ying Zhang(张颖), Yixin Chen(陈一鑫), Kai Sun(孙凯), Daming Chen(陈大明), Qiang Li(李强), Yingli Liu(刘颖力), and Jie Li(李颉)
Chin. Phys. B, 2023, 32 (**9**): 097501. DOI: 10.1088/1674-1056/acc3f7

Hysteresis loss reduction in self-bias FeSi/$SrFe_{12}O_{19}$ soft magnetic composites

Shuangjiu Feng(冯双久), Jiangli Ni(倪江利), Feng Hu(胡锋), Xucai Kan(阚绪材), Qingrong Lv(吕庆荣), and Xiansong Liu(刘先松)
Chin. Phys. B, 2022, 31 (**2**): 027503. DOI: 10.1088/1674-1056/ac2d1a

High-frequency magnetic properties and core loss of carbonyl iron composites with easy plane-like structures

Guo-Wu Wang(王国武), Chun-Sheng Guo(郭春生), Liang Qiao(乔亮), Tao Wang(王涛), and Fa-Shen Li(李发伸)
Chin. Phys. B, 2021, 30 (**2**): 027504. DOI: 10.1088/1674-1056/abc15c

High frequency characteristics of $(Ni_{75}Fe_2)_x(ZnO)_{1-x}$ granular thin films with tunable damping coefficient

Li Wen-Chun (李文春), Zuo Ya-Lu (左亚路), Liu Xiao-Hong (刘晓虹), Wei Qing-Qing (魏清清), Zhou Xue-Yun (周雪云), Yao Dong-Sheng (姚东升)
Chin. Phys. B, 2015, 24 (**4**): 047503. DOI: 10.1088/1674-1056/24/4/047503

RAPID COMMUNICATION

High-frequency complex permeability calculation for metallic soft magnetic particles with easy magnetization plane in non-magnetic medium

Liangrui Tan(谭梁睿)[1], Donglin He(何东霖)[1], Zhibiao Xu(徐志彪)[1], Guowu Wang(王国武)[2], Shengyu Yang(杨晟宇)[1], Shaoyong Leng(冷绍勇)[1], Ruilong Li(李睿龙)[1], and Tao Wang(王涛)[1,†]

[1] *School of Physical Science and Technology, Lanzhou University, Lanzhou* 730000, *China*
[2] *Ninth Institute, China Electronics Technology Group Corporation, Mianyang* 621000, *China*

(Received 4 June 2025; revised manuscript received 30 July 2025; accepted manuscript online 29 August 2025)

Soft magnetic composites made from metallic magnetic particles with an easy magnetization plane (referred to as easy-plane metallic soft magnetic composites (SMC)) are considered ideal materials for the next generation of power electronic devices. This advantage is attributed to their ability to maintain high permeability at elevated frequencies. Despite these advantages, a definitive mathematical model that connects the high-frequency magnetic properties (e.g., effective permeability) of easy-plane metallic SMCs to the intrinsic properties of the particles is still lacking. In this work, a theoretical calculation model for the effective permeability of easy-plane metallic SMCs was formulated. This model was derived from a skin effect-corrected Landau–Lifshitz–Gilbert (LLG) equation and integrated with effective medium theory incorporating inter-particle interaction. To validate the model, we prepared samples of easy-plane Y_2Co_{17} particle/PU SMCs with varying particle sizes and volume fractions. The experimental results showed a strong agreement with the calculated values. This research offers critical theoretical backing for the design and optimization of soft magnetic materials intended for high-frequency applications.

Keywords: easy-plane material, high-frequency, soft magnetic composites, complex permeability, Landau–Lifshitz–Gilbert (LLG) equation

PACS: 75.40.Gb, 85.70.–w, 85.70.Ay

DOI: 10.1088/1674-1056/ae00ad **CSTR:** 32038.14.CPB.ae00ad

1. Introduction

Metallic soft magnetic composites (SMCs), composed of metallic magnetic particles and insulating binders, blend the benefits of high resistivity and saturation magnetization. They find widespread applications in energy transmission and conversion–such as power inductors,[1–6] microwave absorption,[7–9] and information technology, including communication antennas.[10–13] As power electronics and information technology advance, the trend toward miniaturization and high-frequency operation in energy devices, absorbers, and antennas is evident. The demand for high-performance metallic SMCs that sustain high permeability at elevated frequencies is pressing. The efficacy of metallic SMCs hinges on the intrinsic properties of metallic magnetic particles. Studies reveal that metallic magnetic particles with an easy magnetization plane (easy-plane particles) outperform traditional counterparts at higher frequencies.[14–20] Therefore, establishing a theoretical model that links the intrinsic parameters of easy-plane particles (e.g., size, electrical resistivity, saturation magnetization) to the effective permeability of SMCs composed of these particles (easy-plane metallic SMCs) is crucial for optimizing their high-frequency performance.

Recent efforts have delved into the complex permeability characteristics of metallic SMCs.[21–32] Wu *et al.*[33] explored the distribution of particle magnetic moments and effectively determined the permeability of SMCs containing spherical iron particles using effective medium theory. However, their study relied on the conventional Landau–Lifshitz–Gilbert (LLG) equation, rendering it unsuitable for easy-plane metallic SMCs, which exhibit greater potential in high-frequency applications. Additionally, the study's approach to particle magnetic moment orientation had limitations, failing to account for arbitrary magnetic moment orientations and unable to predict the effective permeability of SMCs at high particle loadings. While scholars like Li *et al.*[34] acknowledged the benefits of easy-plane particles and proposed a bi-anisotropic model using the LLG equation to calculate the susceptibility of easy-plane metallic SMCs, this model still has critical limitations, as it inadequately accounts for interparticle interactions and applies only to scenarios with uniformly distributed magnetic moments.

In response to these challenges, this study aims to de-

†Corresponding author. E-mail: wtao@lzu.edu.cn

© 2025 Chinese Physical Society and IOP Publishing Ltd. All rights, including for text and data mining, AI training, and similar technologies, are reserved.

velop a theoretical calculation model for the effective permeability of easy-plane metallic SMCs. This model is composed of two parts: an intrinsic permeability calculation model for easy-plane particles and an effective permeability calculation model tailored to easy-plane metallic SMCs. The model addresses skin effect corrections and the impact of high particle volume fractions. To validate the model, we prepared samples of easy-plane Y_2Co_{17}/PU SMCs with varying particle sizes and volume fractions.

2. Algorithm details

2.1. Algorithm process

Figure 1 illustrates the flowchart detailing our algorithm. We utilized the LLG equation, tailored for easy-plane systems, to calculate the intrinsic permeability of a single easy-plane metallic magnetic particle based on material-specific intrinsic parameters. Subsequently, we considered the magnetic moment distributions of multiple particles to determine the ensemble-averaged permeability. In this step, we employed effective medium theory to determine the effective permeability of easy-plane particle-based SMCs. Notably, our calculations incorporate the particle size effects to accurately account for skin effects.

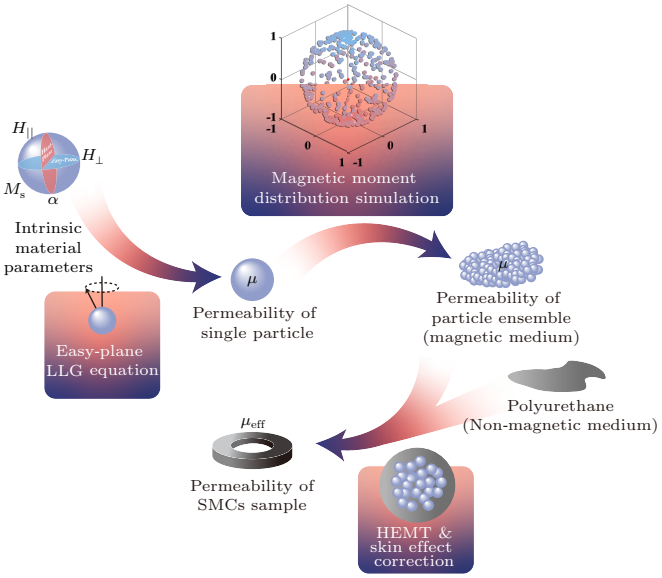


Fig. 1. Flowchart illustrating the calculation of the complex permeability of easy-plane metallic SMCs.

2.2. Calculation of intrinsic permeability for single easy-plane particle

The magnetization $\boldsymbol{M}$ of the magnetic particles is described by the LLG equation[35]

$$\frac{\mathrm{d}\boldsymbol{M}}{\mathrm{d}t} = -\gamma \boldsymbol{M} \times \boldsymbol{H}_{\mathrm{eff}} + \frac{\alpha}{M_{\mathrm{s}}} \boldsymbol{M}_{\mathrm{s}} \times \frac{\mathrm{d}\boldsymbol{M}}{\mathrm{d}t}. \tag{1}$$

Here, γ represents the gyromagnetic ratio, α is the Gilbert damping factor, and M_{s} denotes the saturation magnetization of the particles. The total effective field $\boldsymbol{H}_{\mathrm{eff}} = \boldsymbol{H}_{\mathrm{a}} + \boldsymbol{h}$ includes the static magnetic field $\boldsymbol{H}_{\mathrm{a}}$ and the microwave field $\boldsymbol{h}$.

Considering the easy-plane nature of the particles, the total effective field $\boldsymbol{H}_{\mathrm{eff}}$ can be expressed as[15]

$$\begin{aligned} \boldsymbol{H}_{\mathrm{eff}} = \boldsymbol{h} + \boldsymbol{H}_{\mathrm{a}} &= h_1 \boldsymbol{e}_1 + \left(h_2 - H_{\perp} \frac{M_2}{M_{\mathrm{s}}}\right) \boldsymbol{e}_2 \\ &+ \left(h_3 + H_{\parallel} \frac{M_3}{M_{\mathrm{s}}}\right) \boldsymbol{e}_3. \end{aligned} \tag{2}$$

Here, $H_{\perp}$ and $H_{\parallel}$ denote the out-of-plane and in-plane anisotropy fields, M_i $(i = 1,2,3)$ represent the components of the magnetization $\boldsymbol{M}$ along the principal axes 1, 2, and 3, and h_i $(i = 1,2,3)$ represent the components of the microwave field $\boldsymbol{h}$ along these axes.

By substituting $\boldsymbol{H}_{\mathrm{eff}}$ into the LLG equation, we derive

$$m_1 = \chi_{11} h_1 + \chi_{12} h_2, \quad m_2 = \chi_{22} h_2 - \chi_{12} h_1, \quad m_3 = 0. \tag{3}$$

Here

$$\begin{aligned} \chi_{11} &= \frac{\gamma M_{\mathrm{s}} \left[\gamma \left(H_{\parallel} + H_{\perp}\right) + \mathrm{i}\alpha\omega\right]}{\gamma^2 H_{\parallel} \left(H_{\parallel} + H_{\perp}\right) - \left(1+\alpha^2\right)\omega^2 + \mathrm{i}\alpha\omega\gamma\left(2H_{\parallel} + H_{\perp}\right)}, \\ \chi_{12} &= \frac{\mathrm{i}\omega\gamma M_{\mathrm{s}}}{\gamma^2 H_{\parallel} \left(H_{\parallel} + H_{\perp}\right) - \left(1+\alpha^2\right)\omega^2 + \mathrm{i}\alpha\omega\gamma\left(2H_{\parallel} + H_{\perp}\right)}, \\ \chi_{22} &= \frac{\gamma M_{\mathrm{s}} \left(\gamma H_{\parallel} + \mathrm{i}\alpha\omega\right)}{\gamma^2 H_{\parallel} \left(H_{\parallel} + H_{\perp}\right) - \left(1+\alpha^2\right)\omega^2 + \mathrm{i}\alpha\omega\gamma\left(2H_{\parallel} + H_{\perp}\right)}. \end{aligned} \tag{4}$$

It is important to note that all the above derivations are performed in the particle's principal axis coordinate system o-123. For practical calculations, coordinate transformation is essential to harmonize the results into the laboratory coordinate system. After transformation, the intrinsic permeability of the easy-plane particle is given by[34]

$$\mu = \frac{m_{\mathrm{h}}}{h} + 1 = A^2 \chi_{11} + B^2 \chi_{22} + 1. \tag{5}$$

Here

$$\begin{aligned} A &= \sin\theta \sin\delta \cos\theta_{\mathrm{h}} - \sin\theta_{\mathrm{h}} \left[\cos\theta \sin\delta \cos\left(\varphi_{\mathrm{h}} + \varphi\right)\right], \\ B &= \sin\theta_{\mathrm{h}} \left[\cos\theta \cos\delta \cos\left(\varphi_{\mathrm{h}} + \varphi\right) - \sin\delta \sin\left(\varphi_{\mathrm{h}} + \varphi\right)\right] \\ &\quad - \sin\theta \cos\delta \cos\theta_{\mathrm{h}}, \end{aligned} \tag{6}$$

where θ, ϕ, and δ represent the directional angles of the particle's magnetic moment, while θ_{h} and φ_{h} denote the polar and azimuthal angles of the microwave field in the spherical coordinate system.

2.3. Calculation of the ensemble-averaged permeability

The metallic SMC consists of numerous metallic magnetic powder particles, each of which contributes to the overall permeability. The permeability of an individual particle is influenced by the angle between the microwave field and its

magnetic moment. To accurately calculate the effective permeability of the SMC, the collective influence of all particles in the ensemble must be considered to derive the ensemble-averaged permeability. The intrinsic permeability of a single particle is calculated using Eq. (5), and the ensemble-averaged permeability can be written as

$$\langle \mu \rangle = \sum_{i=1}^{N} \frac{\mu_i(\theta, \varphi)}{N}. \tag{7}$$

Here, $\mu_i(\theta, \varphi)$ represents the intrinsic permeability of an individual particle, and N denotes the total number of particles in the simulation.

2.3.1. Simulation for magnetic moment orientation using Boltzmann distribution function

Traditionally, the magnetic moment distribution of oriented samples has been simulated using a Gaussian distribution. However, the parameters of the Gaussian distribution cannot be directly correlated with physical quantities, thus lacking physical significance. To address this limitation, we propose a magnetic moment distribution model based on the Boltzmann distribution, which establishes the relationship between the orienting magnetic field and the orientation degree of the sample.

The orientation of magnetic moments in magnetic particles within a rotating magnetic field is governed by the interplay between thermodynamic equilibrium and the applied magnetic field. According to the Boltzmann distribution in statistical mechanics, the energy E of a magnetic moment $\boldsymbol{m}$ under the applied magnetic field $\boldsymbol{H}$ is given by

$$E = -\boldsymbol{m} \cdot \boldsymbol{H} = -mH\cos(\theta). \tag{8}$$

Here, $m = |\boldsymbol{m}|$ represents the magnitude of the magnetic moment, $H = |\boldsymbol{H}|$ denotes the strength of the applied magnetic field, and θ is the angle between the magnetic moment and the magnetic field. Owing to the rotational symmetry of the system, the probability density function depends only on the polar angle θ and is independent of the azimuthal angle φ. By incorporating the Boltzmann distribution, the probability density function for the oriented magnetic moment is expressed as

$$P(\theta) = \frac{1}{Z} \mathrm{e}^{\frac{mH\cos(\theta)}{k_\mathrm{B}T}}. \tag{9}$$

Here, k_B is the Boltzmann constant, and T is the absolute temperature. The partition function Z is defined as $Z = \int_0^{2\pi}\int_0^{\pi} \mathrm{e}^{\frac{mH\cos(\theta)}{k_\mathrm{B}T}} \sin(\theta)\,\mathrm{d}\theta\,\mathrm{d}\varphi$. For convenience, the probability density function is written as

$$P(\theta) \propto \sin(\theta)\,\mathrm{e}^{\xi\cos(\theta)}. \tag{10}$$

Here, $\xi = \frac{mH}{k_\mathrm{B}T}$ is a dimensionless parameter characterizing the relative interaction strength between the magnetic moment and the external field. To simulate the distribution of magnetic moments with different orientations, we employ the inverse transform sampling method, which generates random samples from a known cumulative distribution function (CDF).

The CDF for the oriented magnetic moment is expressed as

$$F(\theta) = \int_0^{\theta} P(\theta')\,\mathrm{d}\theta'. \tag{11}$$

Since $P(\theta)$ is the probability density function (PDF) and $F(\theta)$ is the corresponding CDF over the interval [0,1], the inverse cumulative distribution function (ICDF) is defined as the inverse of the CDF

$$F(F^{-1}(u)) = u, \quad u \in [0,1]. \tag{12}$$

For any probability $u \in [0,1]$, $F^{-1}(u)$ returns an angle θ such that $F(\theta) = u$. In practice, direct sampling from the target distribution can be challenging; instead, uniformly distributed random numbers u are generated and transformed into samples x from the target distribution using the ICDF. Due to the typically complex nature of the ICDF, which is often not analytically solvable, we exploit the monotonicity of the CDF to numerically approximate the ICDF via interpolation, thereby improving computational efficiency.

The orientation degree D is defined as the percentage of magnetic moments distributed within a small angle around the xy-plane relative to the total number of magnetic moments, ranging from 0 to 100. Specifically, the orientation degree D is evaluated as

$$D = \frac{M_{xy}}{M} \times 100\%. \tag{13}$$

Here, M is the total number of magnetic moments, and M_{xy} denotes the number of magnetic moments distributed within a small angle around the xy-plane.

Figures 2(a)–2(d) depict the simulation results of magnetic moment distributions at different orientation degrees. In these figures, red dots indicate the centers of unit spheres (radius = 1), while points on the sphere surfaces correspond to the simulated magnetic moment distributions. Vectors extending from the red dots to the surface points indicate the directions of the magnetic moments. Figure 2(e) shows the probability histogram of the magnetic moment distribution across different orientation degrees. For the samples prepared in this study, the random distribution pattern shown in Fig. 2(a) is relevant. A total of 10000 magnetic moments were considered when computing the ensemble-averaged intrinsic permeability of the particles.

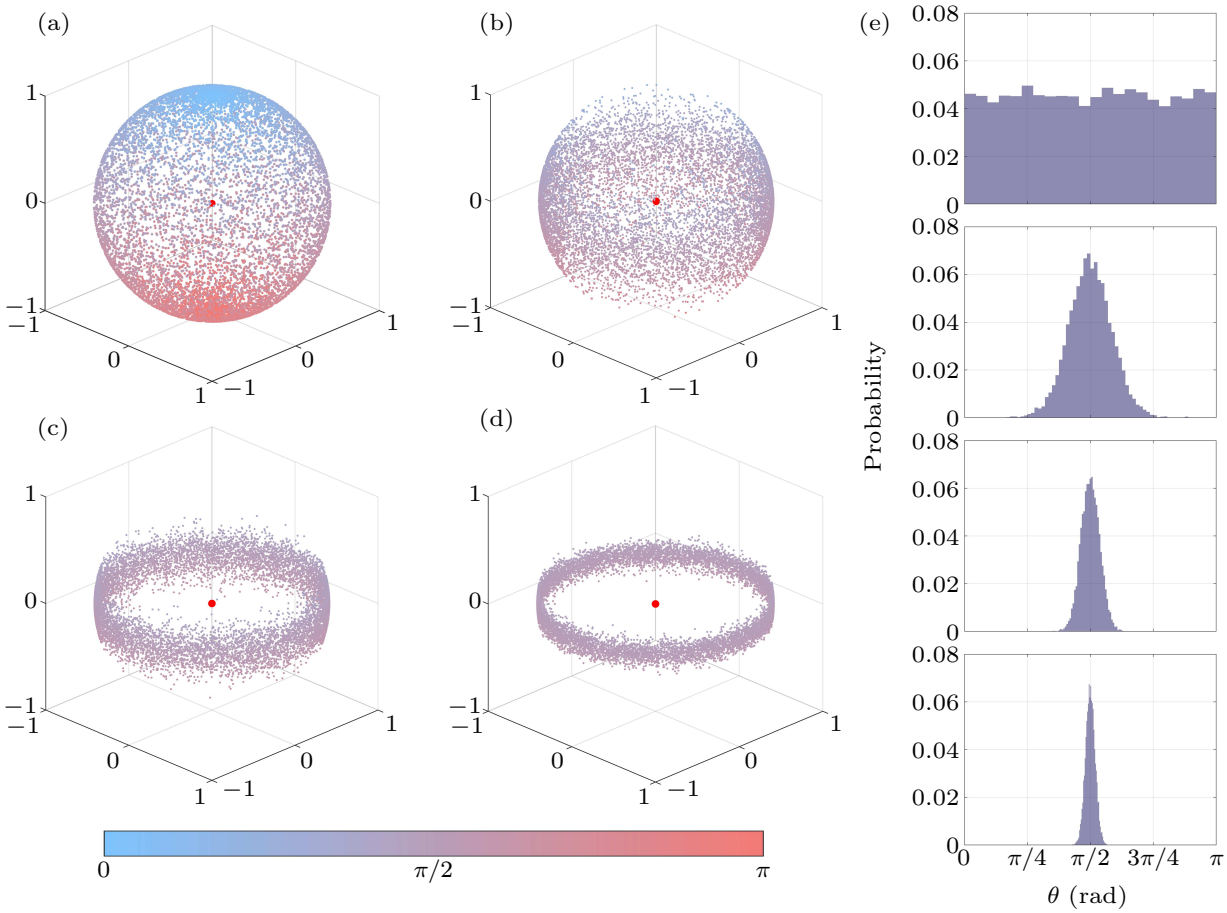


Fig. 2. (a) Schematic illustration of randomly oriented magnetic moments. (b)–(d) Magnetic moment distributions with orientation degrees of 30%, 60%, and 90%, respectively. (e) Histogram showing the probability distribution of magnetic moment orientations at different orientation degrees.

2.4. Effective magnetic permeability calculation for SMC

SMCs can be regarded as systems in which magnetic particles are embedded within a non-magnetic insulating matrix. In such setups, the effective permeability is commonly calculated using effective medium theory (EMT). A commonly used approach is the Bruggeman effective medium theory, formulated as[36,37]

$$f_1 \frac{\mu_1 - \mu_{\text{eff}}}{\mu_1 + 2\mu_{\text{eff}}} + (1 - f_1) \frac{\mu_2 - \mu_{\text{eff}}}{\mu_2 + 2\mu_{\text{eff}}} = 0. \tag{14}$$

Here, f_1 represents the volume fraction of magnetic particles, μ_1 denotes the average permeability of the particle ensemble, μ_2 signifies the permeability of the matrix (with $\mu_2 = 1$ for non-magnetic matrices), and μ_{eff} stands for the effective permeability of the composite.

Although the Bruggeman effective medium theory primarily accounts for mean-field effects, its accuracy decreases at high volume fractions. Yin *et al.*[22] incorporated pairwise particle interactions and employed the Green's function method to solve the local magnetic field. By averaging the local field results, they developed a more accurate effective permeability model, particularly suitable for high-volume fractions and complex microstructures, referred to here as the HEMT. The HEMT is expressed as

$$\mu_{\text{eff}} = \frac{\phi\mu_1 a(1 + \frac{\phi}{4}\beta^2) + (1 - \phi)\mu_0}{\phi\alpha(1 + \frac{\phi}{4}\beta^2) + (1 - \phi)}. \tag{15}$$

Here, $\alpha = \frac{3\mu_0}{\mu_1 + 2\mu_0}$, $\beta = \frac{\mu_1 - \mu_0}{\mu_1 + 2\mu_0}$, ϕ is the volume fraction of magnetic particles, μ_1 denotes the average permeability of the particle ensemble, μ_0 represents the permeability of the matrix (with $\mu_0 = 1$ for non-magnetic matrices), and μ_{eff} is the effective permeability of the composite. In this work, the effective permeability of the composite is calculated using the HEMT.

2.5. Skin effect correction

The skin effect inevitably arises in metallic soft magnetic particles under high-frequency microwave fields. Comsol was employed to simulate the distribution of magnetic field intensity H inside an iron sphere with a radius of 1 μm under a 400 A/m microwave magnetic field. Figures 3(a)–3(d) correspond to the simulation results at microwave magnetic field frequencies of 1 MHz, 10 MHz, 100 MHz, and 1 GHz, respectively. The simulation results show that the magnetic field intensity decays rapidly within the particle and is confined to a surface layer, with this effect becoming more pronounced at

higher microwave frequencies. Therefore, it is vital to incorporate skin effect corrections into the calculations.

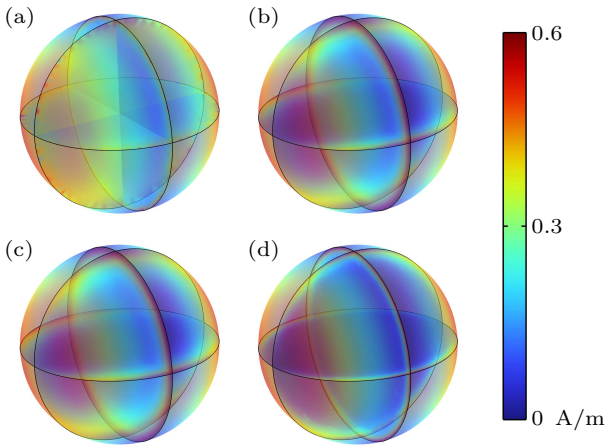


Fig. 3. Simulated magnetic field intensity inside particles under microwave fields at different frequencies: (a) 1 MHz, (b) 10 MHz, (c) 100 MHz, and (d) 1 GHz.

An alternating microwave magnetic field $\boldsymbol{h}_0$ propagates along the Z-axis into the material, and the microwave field $\boldsymbol{h}$ inside the material can be represented as

$$\boldsymbol{h} = \boldsymbol{h}_0 \mathrm{e}^{-z/\delta} \mathrm{e}^{\mathrm{i}(z/\delta - \omega t)}. \tag{16}$$

Here, ω denotes the angular frequency of the microwave. $\mathrm{e}^{-z/\delta}$ is the attenuation factor, where δ stands for the skin depth given by $\delta = \sqrt{\frac{\rho}{\pi \mu_i f}}$, with ρ representing the resistivity, μ_i the intrinsic permeability, and f the microwave frequency. The microwave field gradually attenuates as it penetrates deeper into the material. For spherical particles, the microwave field inside the particle can be expressed as[33]

$$|h| = h_0 \mathrm{e}^{-(R-r)/\delta}, \tag{17}$$

where R represents the particle radius. The particle's dynamic magnetization is expressed as

$$\begin{aligned} \langle m \rangle &= \frac{\sum m}{V} = \frac{\int_0^R \int_0^{2\pi} \int_0^{\pi} h_i \chi_i r^2 \sin\theta \,\mathrm{d}\theta \,\mathrm{d}\phi \,\mathrm{d}r}{V} \\ &= \frac{3h_0\chi_i\delta[R^2 - 2\delta R + 2\delta^2(1-\mathrm{e}^{-R/\delta})]}{R^3}. \end{aligned} \tag{18}$$

Here, χ_i denotes the intrinsic magnetization of the particle. Consequently, the intrinsic permeability of a single particle, including the skin effect, is given by

$$\mu_{i,\mathrm{fix}} = \frac{\langle m \rangle}{h_0} + 1. \tag{19}$$

The average permeability of the particle ensemble, accounting for the skin effect, is calculated as

$$\langle \mu \rangle_{\mathrm{fix}} = \sum_N \frac{\mu_{i,\mathrm{fix}}}{N}. \tag{20}$$

The effective permeability of the metallic SMC, incorporating the skin effect into the HEMT model, is given by

$$\mu_{\mathrm{eff}} = \frac{\phi\mu_1\langle\alpha\rangle_{\mathrm{fix}}(1+\frac{\phi}{4}\langle\beta\rangle_{\mathrm{fix}}^2)+(1-\phi)\mu_0}{\phi\langle\alpha\rangle_{\mathrm{fix}}(1+\frac{\phi}{4}\langle\beta\rangle_{\mathrm{fix}}^2)+(1-\phi)}. \tag{21}$$

Here, $\langle\alpha\rangle_{\mathrm{fix}} = \frac{3\mu_0}{\langle\mu\rangle_{\mathrm{fix}}+2\mu_0}$, $\langle\beta\rangle_{\mathrm{fix}} = \frac{\langle\mu\rangle_{\mathrm{fix}}-\mu_0}{\langle\mu\rangle_{\mathrm{fix}}+2\mu_0}$.

3. Experiment details

3.1. Fabrication

The Y_2Co_{17} alloy, which resembles Co_2Z and exhibits high saturation magnetization, is a prototypical easy-plane metallic soft magnetic material, with magnetization preferentially aligning within the c-crystal plane. This material was chosen to validate the algorithm presented in this work.[38] A series of composite samples containing Y_2Co_{17} powders with varying particle sizes and volume fractions were fabricated, and their complex permeabilities were measured experimentally. The efficacy of the proposed algorithm was confirmed through a comparison between calculated results and experimental data.

The Y_2Co_{17} alloy was prepared by the vacuum induction melting method. The resulting alloy ingot was crushed, ground, and sieved to obtain powders with particle sizes of 100–200 mesh and 400–500 mesh. The powder within the 100–200 mesh category was labeled as BD powder, while the 400–500 mesh Y_2Co_{17} powder underwent ball milling to become SD powder. Ball milling was conducted using 6 mm zirconia balls in n-heptane, with a ball-to-powder ratio of 20:1, at a rotation speed of 200 rpm for 2 hours. To formulate the composites, polyurethane (PU) was used as a binding agent. Oriented samples (used to verify the easy-plane property of Y_2Co_{17}) were prepared by a rotating magnetic field orientation method. For non-oriented samples, the dried SD/BD powders coated with PU were pressed into discs (15 mm in diameter) under a pressure of 340 MPa (approximately 6 tons). The discs were then stamped into toroidal rings (outer diameter = 7 mm, inner diameter = 3 mm) for permeability measurements.

3.2. Characterization

The Y_2Co_{17} powder was analyzed by x-ray diffraction (XRD, Philips, Cu-$K\alpha$ radiation). The morphology of the powders with different particle sizes was examined using scanning electron microscopy (SEM, Thermo Fisher Scientific Apreo S4800). Permeability was measured at room temperature in the frequency range of 1 MHz to 1 GHz using an impedance analyzer (Agilent E4991B), and in the frequency range of 100 MHz to 18 GHz using a vector network analyzer (Agilent Technologies PNA-X N5247A). The hysteresis loop was obtained using a vibrating sample magnetometer

(Lake Shore EV9). To acquire the in-plane and out-of-plane initial magnetization curves for the oriented samples, a superconducting quantum interference device (Quantum Design SQUID-VSM) was utilized.

4. Results and discussion

4.1. Surface morphology, phase composition, and magnetic properties of particles

SEM images of the BD and SD powders are depicted in Figs. 4(a) and 4(b), respectively, unveiling the irregular block-like morphology of the powder particles. Analysis of particle sizes reveals an average size of approximately 120 μm for BD powder and about 5 μm for SD powder. The hysteresis loop illustrated in Fig. 4(c) indicates a saturation magnetization of 132 emu/g and a coercivity of 50 Oe for the Y_2Co_{17} powder, consistent with previous reports.[39] Figure 4(d) presents the XRD pattern of the Y_2Co_{17} powder, displaying good consistency with the standard powder diffraction file card (PDF#97-062-5583), thus confirming the purity of the prepared sample.

To verify the easy-plane property of Y_2Co_{17} and measure the out-of-plane anisotropy field of the SMC, oriented SD/PU composite samples were created. Figure 4(e) illustrates the XRD pattern of the oriented SD/PU composite. Compared with the non-oriented sample, the intensity of the (006) crystal plane peak of oriented Y_2Co_{17} was significantly increased, indicating the alignment of easy magnetization planes of particles parallel to the applied orientation magnetic field. Figure 4(f) depicts the normalized in-plane and out-of-plane initial magnetization curves for the oriented SD/PU composite, highlighting the substantial anisotropy induced by the orientation treatment. Figures 4(e)–4(f) clearly indicate the easy-plane property of Y_2Co_{17}.

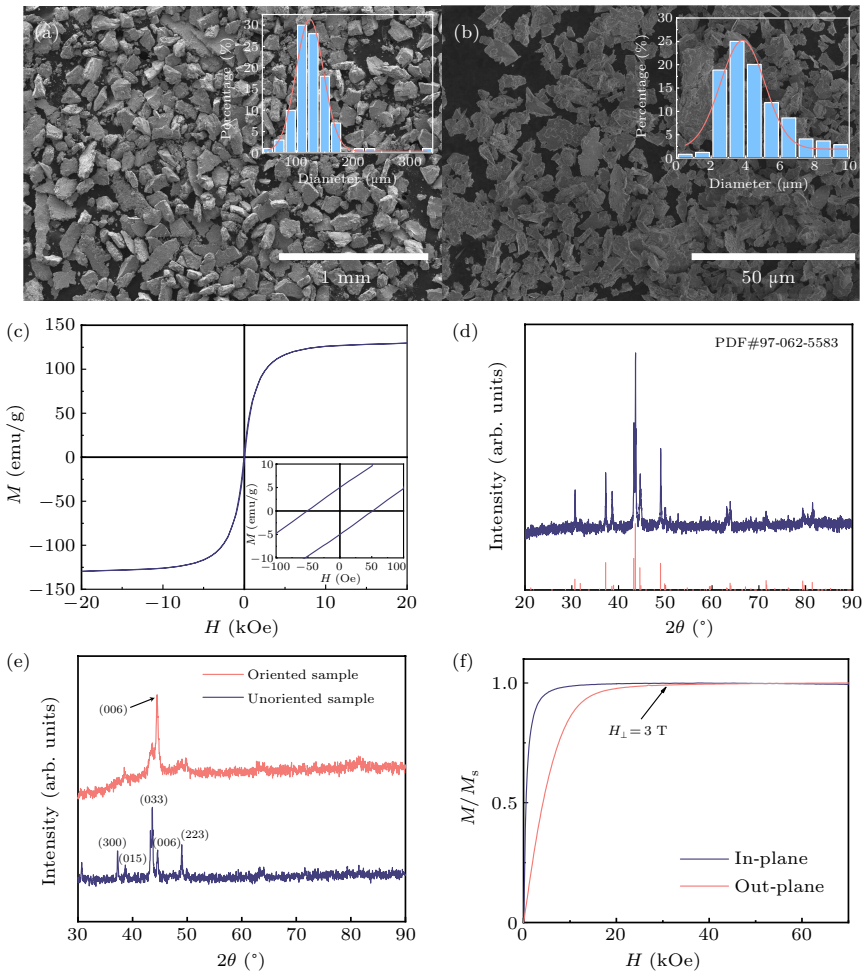


Fig. 4. Characterization of Y_2Co_{17} powders and oriented composites: (a) SEM image of BD powder, (b) SEM image of SD powder, (c) VSM measurement of Y_2Co_{17} powder, (d) XRD pattern of Y_2Co_{17} powder, (e) XRD pattern of the oriented SD/PU composite, and (f) in-plane and out-of-plane initial magnetization curves of the oriented composite.

4.2. Acquisition of in-plane anisotropy field and calculation results

In essence, M_s, $H_\perp$, $H_\parallel$ and a are crucial parameters for calculating the complex permeability of SMCs. As shown in Fig. 4(c), $M_s \approx 1.1 \times 10^6$ A/m (about 132 emu/g). The out-of-plane anisotropy field $H_\perp$ is determined as the intersection field of the in-plane and out-of-plane initial magnetization curves for the oriented SMC,[40] as depicted in Fig. 4(f), where $H_\perp \approx 2.4 \times 10^6$ A/m (roughly 3 T). To extract the in-plane anisotropy field $H_\parallel$, a low-fill sample with a 35% volume

fraction was chosen due to its weak interparticle interaction effect. Figure 5(a) displays the permeability of the 35% volume fraction SD powder composite, exhibiting a natural resonance frequency $f_r = 5.5$ GHz, consistent with the natural resonance frequency formulation for easy-plane systems[15,34]

$$f_r = \frac{\gamma}{2\pi}\sqrt{H_{\parallel}(H_{\perp}+H_{\parallel})}. \tag{22}$$

The corresponding value of $H_{\parallel} \approx 1.01 \times 10^4$ A/m. Our experimental results indicate that a damping coefficient of $a = 0.6$ provides good agreement between experimental and theoretical data.

Various SMCs with volume fractions of 10%, 20%, 25%, 30%, 35%, 40%, 45%, 50%, and 60% were fabricated using SD powder, and their complex permeabilities were measured, providing the real part of the initial permeability for SMCs with differing SD powder loadings. Employing identical material parameters, calculations were performed via both the Bruggeman effective medium theory and our proposed algorithm. Figure 5(b) juxtaposes experimental measurements with theoretical predictions for the real part of the initial complex permeability of SD-based SMC. At lower volume fractions, the Bruggeman theory aligns closely with experimental data. However, as the volume fraction increases, the Bruggeman theory deviates significantly from experimental results, while our algorithm maintains consistent alignment with measurements. Notably, due to constraints related to air gaps in the composites, samples with a maximum volume fraction of 60% were produced in this study. It was found that up to a volume fraction of 80%, the impact on the effective permeability of SMCs was relatively limited. Conversely, beyond a volume fraction of 80%, a significant increase in the effective permeability of SMCs could be achieved by increasing the volume fraction. Hence, optimizing the performance of SMCs in future studies may involve increasing their volume fraction.

Figure 6 presents a comparison between the experimental and calculated complex permeability for 50 vol% Y_2Co_{17}/PU composites fabricated with different particle sizes: (a) BD powder and (b) SD powder. In both panels, the red solid lines signify predictions from our algorithm, while blue dashed lines represent uncorrected predictions that overlook skin effect considerations. As the particle size of the metallic magnetic particles increases, several changes occur: the peak position of the imaginary permeability shifts to lower frequencies, peak broadening occurs, and the cut-off frequency decreases.

Examining the results in Fig. 6(a), significant discrepancies arise between uncorrected calculations and experimental data when skin effects are neglected. In contrast, our algorithm accurately predicts experimental results, underscoring the importance of skin effect corrections for large particle sizes and affirming the efficacy of our approach.

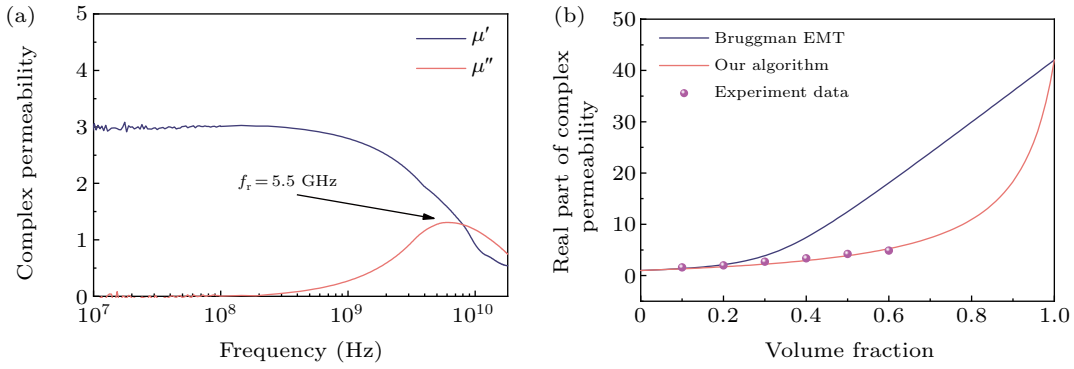


Fig. 5. (a) Complex permeability of SD powder composite with 35% volume fraction. (b) Comparison of experimental and calculated values for the real part of the initial permeability of SD-based SMCs at various volume fractions.

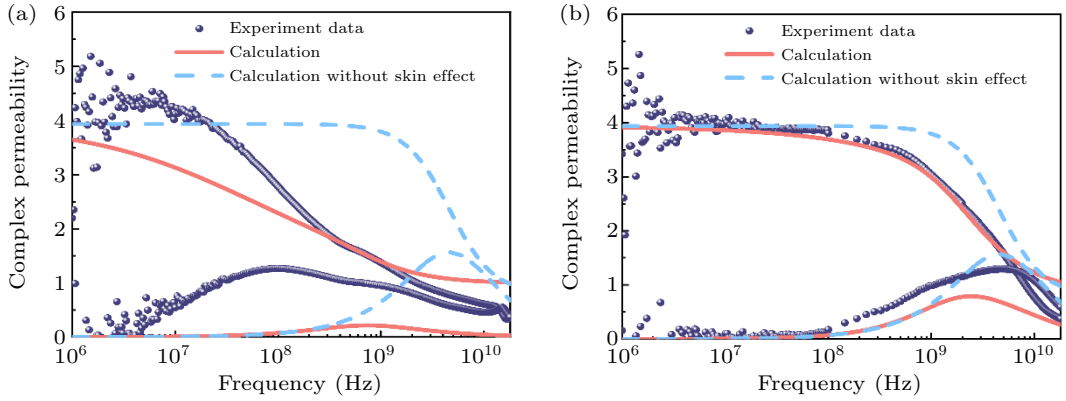


Fig. 6. Comparison of experimental and calculated complex permeability for 50% composite samples: (a) BD powder; (b) SD powder.

Notably, discrepancies exist between predicted complex permeability from our algorithm and experimental values for BD powder composite samples (as depicted in Fig. 6(a)). This deviation is attributed to the single-domain particle assumption adopted in our model. For large-sized magnetic particles, the presence of internal domain walls increases, rendering the single-domain assumption invalid and causing discrepancies between calculated results and experimental data. This phenomenon highlights the necessity of fully considering internal magnetic domain structures when calculating the permeability of large particles.

5. Conclusion

This study introduces a novel algorithm devised to calculate the effective permeability of easy-plane metallic SMC. The intrinsic permeability of particle ensembles was determined using the LLG equation tailored for easy-plane systems, combined with a model for magnetic moment orientation distribution. Subsequently, the HEMT was employed to estimate the effective permeability of the composites. Furthermore, skin effect corrections were incorporated to address the impact of particle size on permeability. Experimental results demonstrate the efficacy of the proposed algorithm in accurately predicting the complex permeability of easy-plane metallic SMC with diverse volume fractions and particle sizes. Based on the experimental findings, future efforts to enhance SMC performance should focus on adjusting the volume fraction, controlling particle size, and regulating anisotropy fields. This study effectively bridges the microscale characteristics of easy-plane metallic SMC (intrinsic particle parameters and distribution states) with their macroscale high-frequency magnetic properties (effective permeability), providing a critical theoretical foundation for the design and optimization of soft magnetic materials in the high-frequency range.

Acknowledgments

This work was supported by the National Key R&D Program of China (Grant No. 2021YFB3501300), the 9th Research Institute of China Electronics Technology Group Corporation's open projects (Grant No. 2024SK-002-01), and the Science and Technology Project of Gansu Province (Grant No. 22YF7GA001).

References

[1] Xu Z B, Wang G W, Zhang S, Cui J H, Xiong L H, He D L, Liu Y and Wang T 2025 *Appl. Phys. Lett.* **126** 082404
[2] Zheng Z L, Feng Q Y, Xiang Q Y, Di Z X and Harris V G 2017 *J. Appl. Phys.* **121** 063901
[3] Shirakata Y, Hidaka N, Ishitsuka M, Teramoto A and Ohmi T 2008 *IEEE Trans. Magn.* **44** 2100
[4] Huang Y D, Zhang H, Shang R X, Wang K, Wu P, Wang Y, Li F S and Wang T 2023 *J. Phys. D: Appl. Phys.* **56** 065004
[5] Li H, Serrano D, Wang S, Guillod T, Luo M and Chen M 2023 *IEEE Applied Power Electronics Conference and Exposition (APEC)*, March 19–23, 2023, Florida, USA, p. 1543
[6] Shen X, Zuo Y, Kong J and Martinez W 2024 *IEEE Trans. Power Electron.* **39** 8478
[7] Zhu Y Y 2023 *J. Magnet. Magnet. Mater.* **570** 170535
[8] Wang Y, Zhang P, Li K, Xin T, Yang W, Liu S, Han J, Du H, Wang C, Luo Z and Yang J 2025 *J. Magnet. Magnet. Mater.* **613** 172677
[9] Wang P 2021 *High-frequency Magnetic and Microwave Absorbing Properties of Rare Earth-transition Metal Alloy Fractured Along Easy-Magnetization Crystal Plane* (Ph.D.Dissertation) (Lanzhou: Lanzhou University) (in Chinese)
[10] Gutfleisch O, Willard M A, Brück E, Chen C H, Sankar S G and Liu J P 2011 *Adv. Mater.* **23** 821
[11] Périgo E A, Weidenfeller B, Kollár P and Füzer J 2018 *Appl. Phys. Rev.* **5** 031301
[12] Silveyra J M, Ferrara E, Huber D L and Monson T C 2018 *Magnet. Mater.* **362** 6413
[13] Krings A, Boglietti A, Cavagnino A and Sprague S 2017 *IEEE Trans. Ind. Electron.* **64** 2405
[14] Rozanov K N, Li Z W, Chen L F and Koledintseva M Y 2005 *J. Appl. Phys.* **97** 13905
[15] Xue D S, Li F S, Fan X L and Wen F S 2008 *Chin. Phys. Lett.* **25** 4120
[16] Wang P, Zhang J, Wang G, Duan B, Wang T and Li F 2020 *Appl. Phys. Lett.* **116** 112403
[17] Wang K, Zhang H, Huang Y D, Xu Z B, Li F S and Wang T 2024 *J. Rare Earths* **42** 110
[18] Xu Z B, Zhang S, Cui J H, He D L, Wang K, Zhao J J, Liu Y and Wang T 2024 *J. Magnet. Magnet. Mater.* **609** 172476
[19] Zhang H, Wang K, Huang Y D, Zhang C H, Wang Y and Wang T 2023 *J. Magnet. Magnet. Mater.* **588** 171471
[20] Wan W, Wu C, Liu G, Chen Q and Yan M 2024 *AIP Adv.* **14** 055213
[21] Han Y, Wang G W, Xu Z B, Wang K, He D L, Wang Y and Wang T 2024 *J. Magnet. Magnet. Mater.* **609** 172467
[22] Yin H M and Sun L Z 2005 *Phys. Rev. B* **72** 054409
[23] Romeis D and Saphiannikova M 2023 *J. Magnet. Magnet. Mater.* **565** 170197
[24] Ntinger B 1994 *Trans. Porous Media* **15** 99
[25] Le Floc'h M, Mattei J L, Laurent P, Minot O and Konn A M 1995 *J. Magnet. Magnet. Mater.* **140–144** 2191
[26] King P R 1989 *Trans. Porous Media* **4** 37
[27] Rousselle D, Berthault A, Acher O, Bouchaud J P and Zérah P G 1993 *J. Appl. Phys.* **74** 475
[28] Bregar V B 2005 *Phys. Rev. B* **71** 174418
[29] Bregar V B and Pavlin M 2004 *J. Appl. Phys.* **95** 6289
[30] Waki H, Igarashi H and Honma T 2005 *IEEE Trans. Magn.* **41** 1520
[31] Liu G, Wang K, Zhang X, Liu H, Luo W, Jin J, Yan M and Wu C 2026 *J. Mater. Sci. Technol.* **245** 197
[32] Wang K, Liu G, Gong J, Wang L, Chen Q, Zhang X, Zhang Z, Yan M and Wu C 2025 *Small* **21** 2501547
[33] Wu L Z, Ding J, Jiang H B, Neo C P, Chen L F and Ong C K 2006 *J. Appl. Phys.* **99** 083905
[34] Li T, Shi H G, Jin X W and Xue D S 2021 *J. Magnet. Magnet. Mater.* **536** 168122
[35] Gilbert T L 2004 *IEEE Trans. Magn.* **40** 3443
[36] Choy T C 2016 *Effective Medium Theory: Principles and Applications* (Oxford: Oxford University Press)
[37] Markel V 2016 *J. Opt. Soc. America A* **33** 1244
[38] Zhong J, Tan G, Man Q, Ning M, Gao Y, Liu X and Pan J 2021 *J. Mater. Sci.: Mater. Electron.* **32** 27849
[39] Andreev A V, Tereshina E A, Gorbunov D I, Šantavá E, Šebek J, Žáček M, Daniš S, Pospíšil J and Havela L 2015 *J. Alloys Compd.* **621** 415
[40] Zhang H, Huang Y D, Wang K, Zhang C H, Wang G W, Li F S and Wang T 2023 *Phys. Scr.* **98** 045917